Pergamon

Int. J. Heat Mass Transfer. Vol. 39, No. 4, pp. 707–715, 1996

0017-9310/96 $15.00 + 0.00

0017-9310(95)00171-9

Local heat transfer in a rotating two-pass ribbed triangular duct with two model orientations

SANDIP DUTTA and JE-CHIN HAN†

Turbine Heat Transfer Laboratory, Department of Mechanical Engineering, Texas A&M University, College Station, TX 77843-3123, U.S.A.

and

C. PANG LEE

General Electric Company, Cincinnati, OH 45215, U.S.A.

(*Received* 29 *December* 1994 *and in final form* 15 *May* 1995)

Abstract—This paper presents experimental heat transfer results in a two-pass triangular duct with ribbed walls. The ribs are placed orthogonal to the bulk flow direction. The rotation is perpendicular to the duct axis. The duct orientation is varied by turning it about its axis with respect to the rotational plane. A change in the duct orientation with respect to the rotating frame causes a change in the secondary flow vortex and turbulence distribution. Consequently, the heat transfer from the individual surfaces changes. The Nusselt number ratio profiles of the six surfaces of the two-pass rib-roughened triangular duct depend on the rotation number. However, heat transfer with ribbed surfaces show different characteristics in rotation number dependency from those with smooth rotating surfaces. Heat transfer from the rib roughened surfaces are modeled by a high-Reynolds number k–ε model and a wall function with sand-roughness. Predictions show different secondary flow vortex structures for two different model orientations.

1. INTRODUCTION

A two-pass rotating duct simulates the conditions of internal serpentine cooling passages in turbine blades. Earlier studies on cooling passages were primarily based on stationary models, which are easier to build and work on. Stationary models neglect the Coriolis and centrifugal buoyancy effects, which affect the velocity, temperature, and turbulence distributions. Rotation causes unstabilization and enhancement of turbulence on one side and stabilization of flow on the other [1]. Location of the unstabilized and stabilized surfaces depend on the flow direction, rotation direction, and the model orientation. Heat transfer from the unstabilized walls are superior compared to that from the stabilized walls [2–5]. Therefore, investigating the heat transfer characteristics of the coolant passages in an actual rotating frame to improve on internal cooling processes in turbine rotor blades is better. Unlike a stationary duct, the model (duct) orientation may significantly affect the heat transfer characteristics in rotation. The Coriolis influenced flow distribution depends on the duct orientation and, consequently, the heat transfer from the individual surfaces changes with the model orientation.

Inclusion of ribs on heat transfer surfaces enhances heat transfer by increasing turbulent mixing and, to some extent, by increasing the participating surface area. The turbulence enhancement by ribs and flow reversal in the separated region interacts with the rotational effects. Ribs and rotation combine to develop a new characteristic in the heat transfer distribution. The present paper is an extension of the works of Dutta *et al.* [6, 7] using smooth walled triangular rotating ducts. The smooth triangular duct of Dutta *et al.* [6, 7] is rib-roughened and heat transfer results for the ribbed duct are obtained at similar operating parameters. Results obtained with ribs show some new characteristics not observed in the smooth duct. FIDAP, a commercial flow and thermal analysis package, is used to predict heat transfer from ribbed walls with the built-in sand-roughness model. The value of the sand-roughness length scale of a particular surface is selected to predict the local heat transfer coefficient at a particular axial location satisfactorily. Predictions for the other axial locations agree well with the measurements.

Earlier works on ribbed rotating ducts were studied with square cross-section models [8–15]. Unlike our observations, effects of rotation on heat transfer in the ribbed square ducts were similar to the rotating smooth walled results in characteristics. Heat transfer increased on unstabilized walls (first pass trailing and second pass leading) and decreased on stabilized walls (first pass leading and second pass trailing) with an increase in the rotation number. The ribbed walls in square ducts were either in the stabilized or unstabilized zone. However, the ribbed walls of our tri-

† Author to whom correspondence should be addressed.

NOMENCLATURE

C_p	specific heat of air [J kg^{-1} K^{-1}]
D	hydraulic diameter [m]
DR	coolant to wall density ratio, $DR = (\rho_{bi} - \rho_w)/\rho_{bi} = (T_w - T_{bi})/T_w$
h	heat transfer coefficient [W m^{-2} °C^{-1}]
Nu	Nusselt number, hD/k
Nu_o	Nusselt number in fully developed turbulent pipe flow
q''_{net}	net heat flux at wall [W m^{-2}]
q''	heat flux at wall [W m^{-2}]
Re, Ro	Reynolds number, $\rho w_o D/\mu$, rotation number, $\Omega D/w_o$
T	temperature [K]
w	axial velocity (in the z-direction) [m s^{-1}]
w_o	average axial flow velocity [m s^{-1}]
z_o	distance measured along the duct axis from the start of heating (m).

Greek symbols

μ	viscosity of air [kg m^{-1} s^{-1}]
Ω	rotational speed of the two-pass channel [rad s^{-1}]
ρ	density of air [kg m^{-3}].

Subscripts

I	inlet values
w	wall values
b	bulk mean values.

angular duct are shared by these two conflicting stabilized and unstabilized rotating flow regions. Moreover, the right triangular duct of our experiment avoids the typical symmetric double-vortex formation of a square duct. Therefore, the results presented are both quantitatively and qualitatively different from earlier published ribbed rotating square duct results. The heat transfer results for several rotation numbers (Ro = 0.22, 0.11, 0.055 and 0.0275) and two model orientations add new knowledge to the thermal sciences.

2. SUMMARY OF EXPERIMENTAL DETAILS

A brief description of the experimental setup and data reduction procedure are included in this section. The experimental rig used by Dutta *et al.* [6, 7] is used here.

2.1. *Experimental facility*

The working fluid is air at atmospheric pressure and room temperature. An orifice meter measures the mean flow rate. The test section rotates in a horizontal plane. The rotating and stationary parts of the setup communicate through rotary couplings and two sets of slip rings. One slip ring unit is for instrumentation and data acquisition. The other is for power supply to the electrical heaters. The rotation speed is measured with a digital photo tachometer.

Figure 1 shows schematics of the top and open views of the two-pass triangular duct. The short and medium surfaces of the triangular passage are 12.7 mm and 25.4 mm, respectively, with an inclusive angle of 90°. The heaters are divided into small isolated rectangular copper pieces to reduce wall conduction effects. Each copper piece is 25.4 mm long, 3 mm thick, and separated by 1.5 mm on all directions from the neighboring pieces. A group of copper elements, laid on any of the six surfaces, share the same input power but each copper element is equipped with individual thermocouple to provide local heat transfer coefficient. The two triangular passes are thermally isolated by Teflon. The heated test section is preceded by an unheated Teflon starting duct, that has the same triangular shape of the test section.

The hydraulic diameter of the triangular test section is 10.2 mm. The test section length to hydraulic diameter ratio is 30, while each pass is 15 hydraulic diameters long connected by a sharp 180° turn. The mean

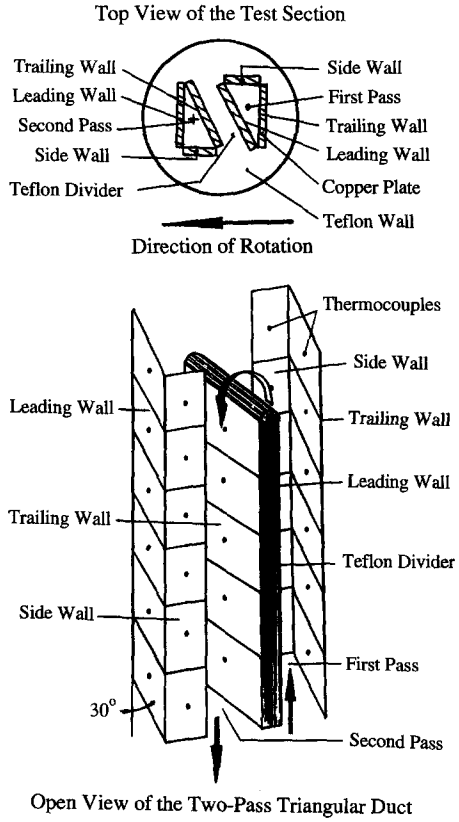

Fig. 1. Illustration of the two-pass triangular duct [6].

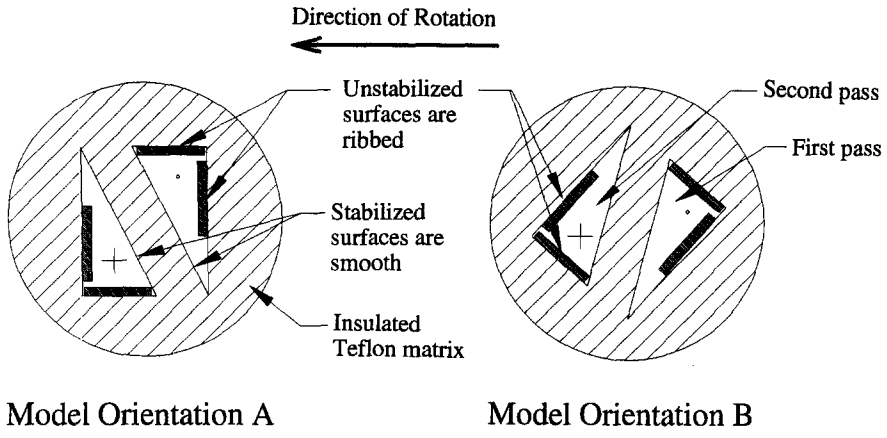

Fig. 2. Two model orientations used.

rotating arm length is 37.5 hydraulic diameters. Four Reynolds numbers (2500, 5000, 10000 and 20000) based on the hydraulic diameter of the channel are used. The duct rotates at 800 rpm, resulting in four rotation numbers (0.22, 0.11, 0.055, 0.0275). The heated walls are at 40°C above ambient giving a density ratio of 0.12. The model orientation is varied by turning the two-pass duct about its own axis. Figure 2 shows two model orientations with respect to the rotation plane. The two model orientations are called Model A and Model B. Figure 2 shows the direction of rotation. The arrow represents the direction of the tangential velocity and not the rotation vector.

Figure 3 shows the predicted velocity distribution in a sand-roughened, one-pass rotating triangular duct for two model orientations. The secondary flow vortex and radial outward flow distribution in the duct are different for the two model orientations. Figure 3 also shows the tentative regions of stabilization and unstabilization of flow in rotation. The ribbed sides

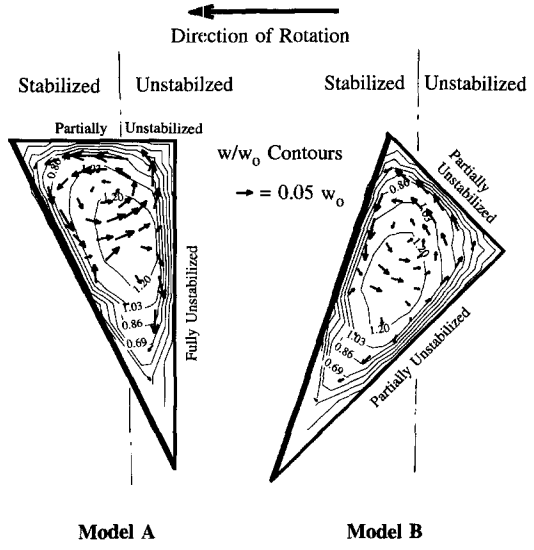

Fig. 3. Predicted flow distribution at $z_o/D = 8$, $Ro = 0.11$ and $DR = 0.12$.

may be fully unstabilized or partially unstabilized by rotation. The effects of full or partial unstabilization on heat transfer are discussed in the results.

2.2. *Rib layout*

Figure 2 shows the surfaces with ribs. The heat transfer from four walls (first pass trailing, second pass leading, and side walls of both passes) increased with rotation for a smooth triangular duct [6, 7]. The enhancement in heat transfer is due to flow unstabilization with rotation near these four surfaces. Ribs are placed on these four unstabilized walls.

The ribs are oriented orthogonal to the bulk flow. Brass ribs of square cross-section are glued to the heater surfaces. The high temperature (insulating) glue thickness is kept to less than 0.3 mm. The rib height to hydraulic diameter ratio is 0.16 and the pitch to height ratio is 10. The ribs on the neighboring surfaces are aligned with each other and not staggered. Zhang *et al.* [16] recommended partial ribbed walls for improved heat transfer characteristics in stationary triangular ducts. Following their recommendation the first pass trailing and second pass leading walls are roughened with half length ribs.

2.3. *Data reduction*

The local heat transfer coefficient is calculated from the local heat flux, the local wall temperature, and the local bulk mean air temperature difference as

$$h = \frac{q''_{\text{net}}}{T_w - T_b}. \quad (1)$$

Local net heat flux (q''_{net}), based on the flat projected area, is obtained by subtracting the heat loss from the power supplied to the heaters. Heat loss is estimated by running a separate test on the same test configuration but without air flow (no-flow condition) in the duct. Characteristic heat loss lines are obtained for each of the isolated rectangular copper pieces. The inlet and outlet openings for the rotating test section are located at more than 120 hydraulic diameters distance from the heated portion of the test duct and do

not interfere with the heat loss test. This no-flow heat loss determination method was tested to be satisfactory on a similar rotating test rig. The local wall temperature (T_w) is obtained from the thermocouple reading of the related heater section. The individual electrical resistive heaters give uniform heat flux heating condition. Therefore, a linear interpolation between the measured inlet (one thermocouple) and outlet (two thermocouples) bulk temperatures gives the local bulk temperature (T_b). The inlet temperature is observed to be higher than the ambient (5–20°C above ambient) and is higher for lower flow rates. This increase in inlet temperature is due to the transfer of heat by conduction to the unheated starting Teflon duct of the test section and the exchange of heat with the outgoing heated air (16–37°C above ambient) from the second pass through the 13 mm thick Teflon divider wall. The calculated and measured outlet bulk mean temperatures are within 3°C and show satisfactory heat balance in the measurements.

To reduce the influence of flow Reynolds number on the heat transfer coefficient, the local Nusselt number is normalized by the Nusselt number for fully developed turbulent flow in smooth stationary pipe, correlated by Dittus-Boelter–McAdams (Rohsenow and Choi [17]) as

$$\frac{Nu}{Nu_o} = \frac{hD}{k_{air}} \frac{1}{(0.023 Re^{0.8} Pr^{0.4})}. \quad (2)$$

The Prandtl number, Pr, for air is 0.72. The value of thermal conductivity of air, k_{air}, is taken at the average of the inlet and outlet bulk mean air temperatures.

2.4. *Uncertainty*

The uncertainty of the local heat transfer coefficient depends on the uncertainties in the local wall and bulk air temperature difference and the net heat input for each test section. This uncertainty increases with decreases in either the local wall-to-air temperature difference or the net heat flux. The net heat flux is higher in a ribbed duct than in a smooth duct and, therefore, the uncertainty of the ribbed duct results is less than the smooth duct results. Based on the method described by Kline and McClintock [18], the typical uncertainty in the Nusselt number is estimated to be $<5\%$ for Reynolds numbers larger than 5000. The maximum uncertainty, however, could be up to 15% for the lower heat transfer coefficient at the lowest Reynolds number tested ($Re = 2500$).

3. SUMMARY OF NUMERICAL DETAILS

Predictions are made with a standard k–ε model of a commercial finite element analysis package, FIDAP (Version 7.05) of Fluid Dynamics International, Inc. Galerkin formulation for the method of weighted residuals is used. The pressure and velocity link has been solved by the penalty function approach. Numerical predictions of this work give insight to the flow distribution and help to interpret the experimental heat transfer results. New numerical model development is not within the scope of this paper.

3.1. *Features added to the standard* k–ε *model*

The standard high Reynolds number k–ε model is expanded to include the rotational and roughness effects. The model equations are listed in Dutta *et al.* [6]. The first pass of the two-pass duct is modeled with a radial outward flow condition. Key features added to the standard three-dimensional (3D) k–ε model include:

(1) Coriolis effects in axial main-flow (w) momentum and cross-flow momentum equations;
(2) the centrifugal buoyancy effect, by assigning a rotational acceleration of $\Omega^2 R$;
(3) generation of turbulent kinetic energy from the buoyancy effect and
(4) wall function with sand-roughness model.

3.2. *Heat transfer calculations*

The heat transfer calculations are done based on the universal law of the walls (wall function) with sand-roughness as given in the FIDAP manual (Version 7). The non-dimensional distance of the near wall node from the wall, y^+, and the friction velocity, u_*, are given as

$$y^+ = \frac{\rho y}{\mu} u_* \quad u_* = C_\mu^{0.25} k^{0.5}. \quad (3)$$

The near wall velocity profiles with sand-roughness (y_o) are given by the FIDAP manual as:

$$u^+ = \frac{1}{\kappa + a} \ln(1 + (\kappa + a) y^+) + (7.8 + c - \delta u^+) d_1$$

$$\text{for } y^+ \leqslant y_o^+$$

$$u^+ = \frac{1}{\kappa} \ln(1 + a y_o^+ + \kappa y^+) + (7.8 - \delta u^+) d_1$$

$$\text{for } y^+ > y_o^+ \quad (4)$$

where y_o^+ is the non-dimensional roughness length scale, $y_o^+ = \rho u_* y_o / \mu$ and y_o is the sand-roughness. Moreover, in the preceding equation

$$d_1 = 1 - \exp(-y^+/11) - (y^+/11) \exp(-0.33 y^+)$$

$$d_2 = 1 - \exp(-y_o^+/70)$$

$$a = 0.15 d_2 \quad c = \left(\frac{1}{\kappa} - \frac{1}{\kappa + a}\right) \ln(1 + (\kappa + a) y_o^+). \quad (5)$$

The shift in the velocity profile resulting from roughness is given by:

$$\delta u^+ = \frac{1}{\kappa} \ln(1 + \kappa d_2 y_o^+) - 0.7 d_2. \quad (6)$$

The temperature profile at the near wall region is governed by the near wall velocity profile and is given by:

$$T^+ = \frac{\rho C_p (T - T_w)}{q''} u_* = Pru^+ D_T + Pr_t(1 - D_T)(u^+ + P_T) \quad (7)$$

where

$$D_T = \exp\left[-\frac{y^+}{11} (Pr/Pr_t)^{0.333} \right] \quad (8)$$

where κ and Pr_t are taken as 0.41 and 0.9, respectively. P_T is defined by Jayatilleke [19] as

$$P_T = 9.24[(Pr/Pr_t)^{0.75} - 1] \times \left[1 + 0.28 \exp\left(-0.007 \frac{Pr}{Pr_t} \right) \right]. \quad (9)$$

Nusselt number calculations are performed as

$$Nu = \frac{q'' D}{(T_w - T_b) k_{air}} \quad (10)$$

where q'' is the average heat flux in the related surface at the desired axial (z-direction) location and k_{air} is the thermal conductivity of air. The bulk temperature, T_b, is calculated by the usual mass-average technique.

3.3. *Computation domain and boundary conditions*

The triangular duct cross-section is discussed in an earlier section of this paper. Unlike the experimental setup, the duct modeled is one-pass with radially outward flow at $Re = 50\,000$ and $Ro = 0.11$. Predictions for $Re = 5000$ and $Ro = 0.11$ (like experiment) could not be achieved because the roughness length scale required for satisfactory prediction of $Re = 5000$ is more than the hydraulic diameter of the duct. The length scales required for $Re = 50\,000$ are more reasonable. The Reynolds number of the numerical flow is obtained by a 10-times higher density of air (similar to compressed air). Therefore, the air bulk flow velocity and the rotation speed (i.e. the rotation number) of the numerical model are the same as those of the experiment. The duct modeled is 50 hydraulic diameters long. The predictions presented are for 30–45 hydraulic diameters corresponding to a mean rotating radius of 37.5 hydraulic diameters. Uniform axial velocity and zero cross-stream velocities are assigned at the inlet. The k and ε at the inlet are given as $k = 0.2\%$ of w_c^2 and $\varepsilon = C_\mu k^{1.5}/D$. Due to an unheated starting length of 30 hydraulic diameters, the predictions are sufficiently independent of the inlet conditions. The three walls are maintained at $DR = 0.12$ from 30 hydraulic diameters. Standard outflow conditions are given at the outlet.

The wall roughness is simulated by a sand-roughness model available in FIDAP. Table 1 shows the assigned sand-roughness length scales, y_o, for individual surfaces with two model orientations. Roughness length scales (y_o) were selected to match numerical predictions with experimental heat transfer data at a specific location of the triangular duct. To avoid influences of the inlet and outlet conditions, roughness calibration is done at $z_o/D = 3.8$. Selected roughness values (y_o) reflect not only the rib roughness effect but also the turbulence enhancement by rotation. Roughness length scales (y_o) of trailing and side walls are dependent on the model orientation due to the rotational effects. Moreover, roughness is required for the smooth leading wall to simulate the enhanced turbulence mixing in the entire duct by ribs.

Table 1. Sand-roughness length scales (y_o)

Model orientation	Leading wall [mm]	Trailing wall [mm]	Side wall [mm]
A	0.1	1.6	0.75
B	0.1	1.2	1.2

3.4. *Grid independence and convergence criteria*

Computations are done on 3D brick elements with eight nodes. Two grid densities with 880 and 1700 nodal points are tested for grid independence. The Nusselt numbers predicted by the two grid densities are within 15% of each other. Grid dependence was more satisfactory and less than 10% for smooth wall predictions [6, 7]. The results presented are with 1700 nodal points. With rotational terms included in the momentum equations, the standard convergence criterion of mass residue fails to work. This is related to the way the program handles pressure at the exit plane. Therefore, spot values are monitored and less than a 0.5% variation is observed for the flow related quantities at the region of interest (30–45 hydraulic diameters) in the last 10 iterations. Note that the finite element procedure takes fewer iterations to converge than required for the finite difference method. Therefore, almost no change in the solution in the last 10 iterations for a finite element formulation can be considered as a convergence criterion.

4. RESULTS AND DISCUSSION

Experimental and numerical heat transfer results are presented in this paper. The effect of rotation on heat transfer is discussed first, followed by the effect of model orientation and effect of rotation number on heat transfer. Comparisons of the numerical results with the experimental data are given at the end of this section.

4.1. *Effect of rotation on heat transfer*

Figures 4(a)–(d) present the Nusselt number ratios (Nu/Nu_o) at four different Reynolds numbers (Re). Both non-rotating stationary ($Ro = 0$) and with 800 rpm rotation ($Ro > 0$) heat transfer results for individual surfaces are included in the plots. Heat transfer from the ribbed walls (first pass trailing, second pass leading and the side walls) are much higher than the smooth walls (first pass leading and second pass trailing walls). The effects of rotation on heat transfer is more prominent for the lower Reynolds number flows ($Re = 2500$ and 5000) with higher rotation numbers ($Ro = 0.22$ and 0.11). Figures 4(a) and (b) show that

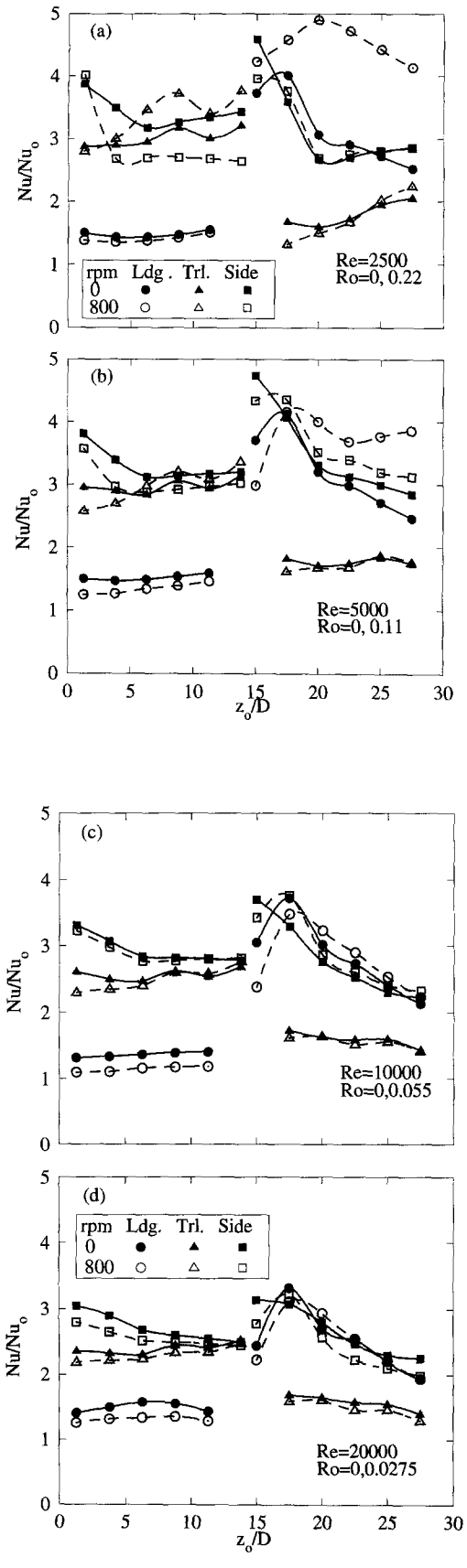

Fig. 4. Axial distribution of span-averaged Nusselt number ratio.

rotation enhances heat transfer from the first pass trailing and second pass leading walls. However, the first pass leading and second pass trailing walls show a decrease in the Nusselt number ratio with rotation. Heat transfer from the first pass side wall decreases with rotation and the second pass side wall heat transfer either stays the same ($Re = 2500$) or increases ($Re = 5000$). At higher Reynolds numbers ($Re = 10\,000$ and $20\,000$) with lower rotation numbers ($Ro = 0.055$ and 0.0275), effects of rotation on heat transfer are not significant on the ribbed walls.

4.2. *Effect of model orientation on heat transfer*

Figures 5(a)–(d) show the effects of model orientation on heat transfer. Heat transfer from the individual surfaces of the rotating triangular two-pass duct with model orientations A and B is shown. Heat transfer from smooth first pass leading and second pass trailing walls are not significantly affected by the model orientation. In rotation, the bulk flow and turbulence increase near the unstabilized sides. In Model A, first pass trailing and the second pass leading are unstabilized sides. However, in Model B, the unstabilization effect of rotation is shared by the first pass trailing and side walls, and second pass leading and side walls (see Fig. 3). Heat transfer enhancement by rotational unstabilization is reflected in the heat transfer patterns. Model A has higher heat transfer coefficient in the first pass trailing and the second pass leading walls than that in Model B. However, the heat transfer from the side walls at both passes shows mostly an increase with Model B than Model A.

4.3. *Effect of rotation number on heat transfer*

Figure 6 shows the effect of rotation number (Ro) on the Nusselt number ratio (Nu/Nu_o) for Model A. The ribbed duct results are compared with smooth walled results of Dutta *et al.* [7]. The first pass trailing and second pass leading walls show an increase in the Nusselt number ratio with an increase in the rotation number. The influence of rotation number on heat transfer from the side walls is mixed. There is an increase in the heat transfer from the side walls at low rotation numbers from the corresponding no-rotation case. At a higher rotation number ($Ro = 0.22$), the side wall Nusselt number ratio (Nu/Nu_o) decreases from the previous rotation number value. Inclusion of ribs enhances turbulence in the duct and heat transfer from the smooth first pass leading and second pass trailing walls of the ribbed duct is more than with all smooth walls.

Figure 7 shows the effect of rotation number on heat transfer with model orientation B. Smooth wall results from Dutta *et al.* [7] are included for comparison. Smooth wall results show an increase in heat transfer from the first pass trailing, second pass leading, and the side walls with an increase in rotation number. The ribbed duct results show that the heat transfer from those surfaces increases with rotation number at low rotation numbers but decreases at

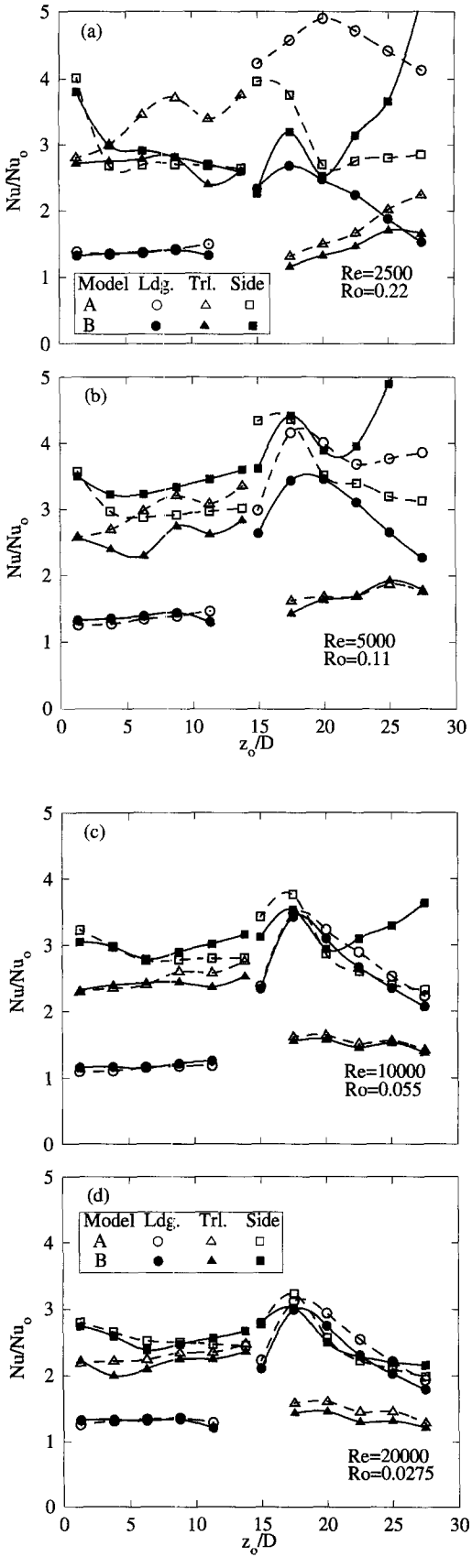

Fig. 5. Axial distribution of span-averaged Nusselt number ratio.

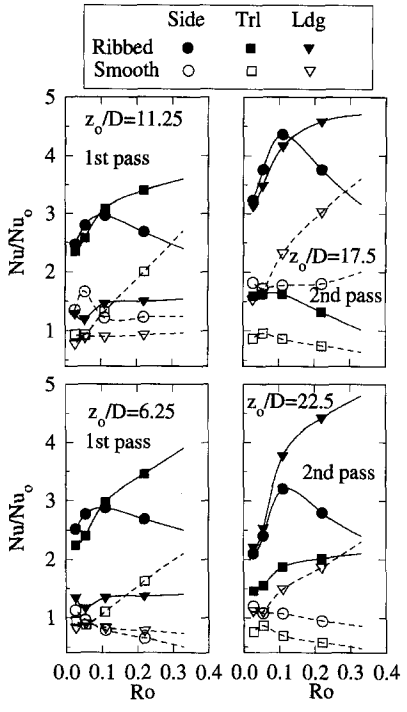

Fig. 6. Heat transfer dependency on rotation number with model orientation A.

higher rotation numbers. It can be argued that the increase and decrease in Nusselt number ratio (Nu/Nu_o) with an increase in rotation number (Ro) is linked to the spiral path line of the fluid particles caused by the rotation induced secondary flow. The

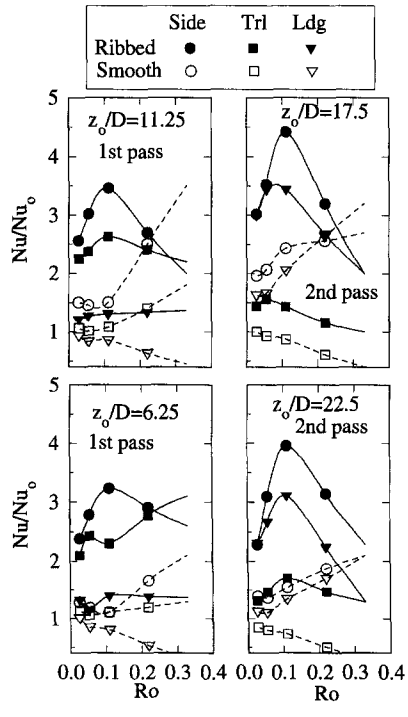

Fig. 7. Heat transfer dependency on rotation number with model orientation B.

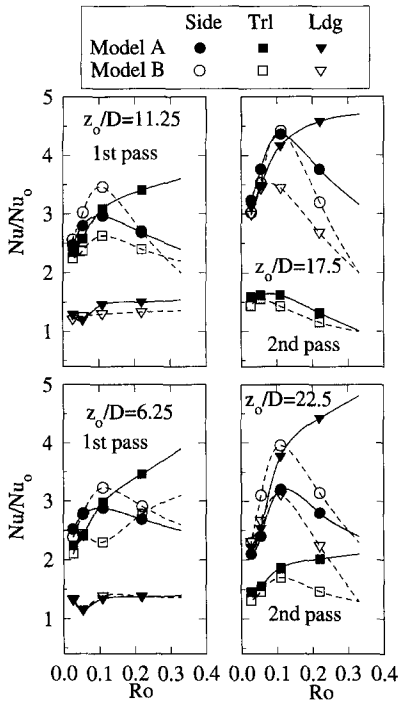

Fig. 8. Effect of model orientation on rotation number dependency of rib-enhanced Nusselt number ratio.

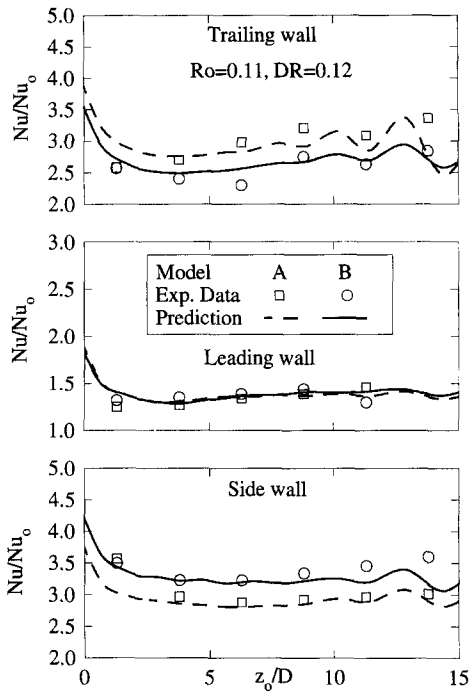

Fig. 9. Prediction of axial distribution of span-averaged Nusselt number ratio.

angle of approach of the flow with respect to the rib orientation is dependent on the rotation number and perhaps the angle of approach is not favorable for heat transfer enhancement beyond a certain rotation number for partially unstabilized surfaces.

Figure 8 shows the effects of rotation number on the Nusselt number ratio for two model orientations. It can be seen that the model orientation can significantly influence the heat transfer pattern. In Model A, the first pass trailing wall and the second pass leading wall can be considered as fully unstabilized by rotation (see Fig. 3). However, the side walls of both passes in Model A are partially unstabilized because the side walls are neither trailing nor leading walls. A similar analogy shows that all four ribbed walls are partially unstabilized by rotation in Model B. Figure 8 shows that the effect of rotation number on the Nusselt number ratio for the partially unstabilized surfaces bears a similarity with each other. Nusselt number ratio from the partially unstabilized surfaces decrease at the highest rotation number experimented ($Ro = 0.22$) compared to the previous rotation number ($Ro = 0.11$) Nusselt number ratio. However, the Nusselt number ratio for the fully unstabilized walls increases monotonically with rotation number.

4.4. *Numerical prediction of heat transfer*

Figure 9 shows the model predictions for $Re = 50\,000$ (same velocity but 10 times the air density used in experiments) and $Ro = 0.11$. The predictions are with a sand-roughness model. Experimental results for $Re = 5000$ with the same rotation number and density ratio are plotted along with the numerical predictions. The predictions show that the heat transfer from ribbed ducts can be effectively modeled by sand-roughened surfaces. However, the value of the sand-roughness depends on the rib roughness and rotational effects on turbulence enhancement. Prior calibration of the roughness length scale is required for a reasonable prediction. Note that heat transfer from $z_0/D = 3.8$ is used for calibration of the sand-roughness. The predictions show that this sand-roughness, calibrated for a specific location, gives satisfactory prediction for the entire heat transfer region.

5. CONCLUSIONS

An experimental heat transfer study is done on a two-pass triangular duct with rib-roughened walls. The duct rotates about an axis orthogonal to its own. The model orientation of the two-pass duct is varied to influence the heat transfer characteristics from the individual surfaces. The experimental study shows that the characteristic dependence of the Nusselt number ratio on the rotation number is different for ribbed walls from that of all smooth walls in similar flow, rotation and model orientations. The fully unstabilized ribbed sides show an increase in the Nusselt number ratio with an increase in the rotation number. Whereas, the Nusselt number ratio of partially unstabilized ribbed sides shows a mixed dependence on the rotation number. The Nusselt number ratio on the partially unstabilized sides increase with an increase in the rotation number at lower rotation number

operating conditions. This increase is followed by a decrease in Nusselt number ratio for the partially unstabilized surfaces with a further increase in rotation number. Numerical predictions with a k–ε model of a commercial code is presented for a better understanding of the problem. The predictions show that heat transfer with complicated flow separation and rotation can be modeled with a simple sand-roughness approach with prior calibration of the roughness length scale.

Acknowledgements—This experimental work was sponsored by General Electric Aircraft Engines. The numerical work was supported by a research grant of computer time allocated by the Supercomputing Center, Texas A&M University, College Station, Texas. Their support is gratefully acknowledged.

REFERENCES

1. J. P. Johnston, R. M. Halleen and D. K. Lezius, Effects of spanwise rotation on the structure of two-dimensional fully developed turbulent channel flow, *J. Fluid Mech.* **56**(3), 533–557 (1972).
2. J. H. Wagner, B. V. Johnson and T. J. Hajek, Heat transfer in rotating passages with smooth walls and radial outward flow, *ASME J. Turbomachinery* **113**, 42–51 (1991).
3. J. H. Wagner, B. V. Johnson and F. C. Kopper, Heat transfer in rotating serpentine passages with smooth walls, *ASME J. Turbomachinery* **113**, 321–330 (1991).
4. J. C. Han, Y. M. Zhang and C. P. Lee, Influence of surface heating condition on local heat transfer in a rotating square channel with smooth walls and radial outward flow, *ASME J. Turbomachinery* **116**(1), 149–158 (1994).
5. J. C. Han, Y. M. Zhang and K. Kalkuehler, Uneven wall temperature effect on local heat transfer in a rotating two-pass square channel with smooth walls, *ASME J. Heat Transfer* **115**(4), 912–920 (1993).
6. S. Dutta, J. C. Han, Y. M. Zhang and C. P. Lee, Local heat transfer in a rotating two-pass triangular duct with smooth walls, ASME paper No. 94-GT-337. *ASME J. Turbomachinery* (accepted).
7. S. Dutta, J. C. Han and C. P. Lee, Effect of model orientation on local heat transfer in a rotating two-pass smooth triangular duct, 1994 Winter Annual Meeting, Chicago, Illinois, 6–11 November, ASME HTD-Vol. 300, pp. 147–153; *ASME J. Heat Transfer* (in press).
8. J. H. Wagner, B. V. Johnson, R. A. Graziani and F. C. Yeh, Heat transfer in rotating serpentine passages with trips normal to the flow, *ASME J. Turbomachinery* **114**, 847–857 (1992).
9. M. E. Taslim, L. A. Bondi and D. M. Kercher, An experimental investigation of heat transfer in an orthogonally rotating channel roughened with 45 degree criss-cross ribs on two opposite walls, *ASME J. Turbomachinery* **113**, 346–353 (1991).
10. M. E. Taslim, A. Rahman and S. D. Spring, An experimental investigation of heat transfer coefficients in a spanwise rotating channel with two opposite rib-roughened walls, *ASME J. Turbomachinery* **113**, 74–82 (1991).
11. J. A. Parsons, J. C. Han and Y. M. Zhang, Wall heating effect on local heat transfer in a rotating two-pass square channel with 90° rib turbulators, *Int. J. Heat Mass Transfer* **37**(9), 1411–1420 (1994).
12. S. Fann, W. J. Yang and N. Zhang, Local heat transfer in a rotating serpentine passage with rib-roughened surfaces, *Int. J. Heat Mass Transfer* **37**(2), 217–228 (1994)
13. B. V. Johnson, J. H. Wagner, G. D. Steuber and F. C. Yeh, Heat transfer in rotating serpentine passages with selected model orientations for smooth or skewed trip walls, *ASME J. Turbomachinery* **116**(4), 738–744 (1994).
14. B. V. Johnson, J. H. Wagner, G. D. Steuber and F. C. Yeh, Heat transfer in rotating serpentine passages with trips skewed to the flow, *ASME J. Turbomachinery* **116**(1), 113–123 (1994).
15. J. A. Parsons, J. C. Han and Y. M. Zhang, Effects of model orientation and wall heating condition on local heat transfer in a rotating two-pass square channel with rib turbulators, *Int. J. Heat Mass Transfer* **38**(7), 1151–1159 (1995).
16. Y. M. Zhang, W. Z. Gu and J. C. Han, Augmented heat transfer in triangular ducts with full and partial ribbed walls, *AIAA J. Thermophys. Heat Transfer* **8**(3), 574–579 (1994).
17. W. M. Rohsenow and H. Choi, *Heat, Mass and Momentum Transfer*, pp. 192 and 193. Prentice-Hall, New Jersey (1961).
18. S. J. Kline and F. A. McClintock, Describing uncertainties in single-sample experiments, *Mech. Engng*, pp. 3–8 (1953).
19. C. L. V. Jayatilleke, The influence of Prandtl number and surface roughness on the resistance of the laminar sub-layer to momentum and heat transfer, *Prog. Heat Mass Transfer* **1**, 193–329 (1969).